



# Porous Hollow Superlattice NiMn<sub>2</sub>O<sub>4</sub>/NiCo<sub>2</sub>O<sub>4</sub> Mesocrystals as a Highly Reversible Anode Material for Lithium-Ion Batteries

Lingjun Li<sup>1,2\*</sup>, Qi Yao<sup>1</sup>, Jiequn Liu<sup>3</sup>, Kaibo Ye<sup>1</sup>, Boyu Liu<sup>1</sup>, Zengsheng Liu<sup>1</sup>, Huiping Yang<sup>1</sup>, Zhaoyong Chen<sup>1</sup>, Junfei Duan<sup>1</sup> and Bao Zhang<sup>4\*</sup>

<sup>1</sup> School of Materials Science and Engineering, Changsha University of Science and Technology, Changsha, China, <sup>2</sup> Hunan Provincial Key Laboratory of Efficient and Clean Energy Utilization, Changsha University of Science and Technology, Changsha, China, <sup>3</sup> School of Iron and Steel, Soochow University, Suzhou, China, <sup>4</sup> School of Metallurgy and Environment, Central South University, Changsha, China

## OPEN ACCESS

### Edited by:

Qiaobao Zhang,  
Xiamen University, China

### Reviewed by:

Xiao-Dong Zhu,  
Harbin Institute of Technology, China  
Baihua Qu,  
Xiamen University, China  
Cao Guan,  
National University of Singapore,  
Singapore

### \*Correspondence:

Lingjun Li  
lingjun.li@csust.edu.cn  
Bao Zhang  
csuzb@vip.163.com

### Specialty section:

This article was submitted to  
Physical Chemistry and Chemical  
Physics,  
a section of the journal  
Frontiers in Chemistry

Received: 13 March 2018

Accepted: 18 April 2018

Published: 15 May 2018

### Citation:

Li L, Yao Q, Liu J, Ye K, Liu B, Liu Z, Yang H, Chen Z, Duan J and Zhang B (2018) Porous Hollow Superlattice NiMn<sub>2</sub>O<sub>4</sub>/NiCo<sub>2</sub>O<sub>4</sub> Mesocrystals as a Highly Reversible Anode Material for Lithium-Ion Batteries. *Front. Chem.* 6:153. doi: 10.3389/fchem.2018.00153

As a promising high-capacity anode material for Li-ion batteries, NiMn<sub>2</sub>O<sub>4</sub> always suffers from the poor intrinsic conductivity and the architectural collapse originating from the volume expansion during cycle. Herein, a combined structure and architecture modulation is proposed to tackle concurrently the two handicaps, via a facile and well-controlled solvothermal approach to synthesize NiMn<sub>2</sub>O<sub>4</sub>/NiCo<sub>2</sub>O<sub>4</sub> mesocrystals with superlattice structure and hollow multi-porous architecture. It is demonstrated that the obtained NiCo<sub>1.5</sub>Mn<sub>0.5</sub>O<sub>4</sub> sample is made up of a new mixed-phase NiMn<sub>2</sub>O<sub>4</sub>/NiCo<sub>2</sub>O<sub>4</sub> compound system, with a high charge capacity of 532.2 mAh g<sup>-1</sup> with 90.4% capacity retention after 100 cycles at a current density of 1 A g<sup>-1</sup>. The enhanced electrochemical performance can be attributed to the synergistic effects of the superlattice structure and the hollow multi-porous architecture of the NiMn<sub>2</sub>O<sub>4</sub>/NiCo<sub>2</sub>O<sub>4</sub> compound. The superlattice structure can improve ionic conductivity to enhance charge transport kinetics of the bulk material, while the hollow multi-porous architecture can provide enough void spaces to alleviate the architectural change during cycling, and shorten the lithium ions diffusion and electron-transportation distances.

**Keywords:** lithium-ion battery, transition metal oxide, superlattice structure, hollow multi-porous architecture, electrochemical kinetics

## INTRODUCTION

Nowadays, Graphite-based materials are the main anode material for current commercial lithium-ion battery (LIB) (Kang et al., 2006; Scrosati et al., 2011; Xie et al., 2012; Goodenough and Park, 2013; Yuan et al., 2014; Yan et al., 2017). However, the low theoretical specific capacity of 372 mAh g<sup>-1</sup> and poor rate capability limit its application in next generation high energy density LIB (Mai et al., 2011; Pan et al., 2014; Liu et al., 2015; Ma Z. et al., 2015; Wang J. X. et al., 2016; Wu et al., 2017; Su et al., 2018). In this regard, a variety of simple metal oxides, such as tin oxide, manganese oxide, iron oxide and cobalt oxide with high energy density, have drawn much attention as the desired candidates for anode materials to satisfy the high energy storage requirements (Mai et al., 2011; Xie et al., 2012; Li Q. et al., 2013; Pan et al., 2014; Yuan et al., 2014; Liu et al., 2015; Ma Z. et al., 2015; Wang J. X. et al., 2016; Yan et al., 2017; Su et al., 2018). In addition, complex oxides,

such as NiMn<sub>2</sub>O<sub>4</sub>, ZnCo<sub>2</sub>O<sub>4</sub>, CoMn<sub>2</sub>O<sub>4</sub>, ZnFe<sub>2</sub>O<sub>4</sub>, CuCo<sub>2</sub>O<sub>4</sub>, and ZnMn<sub>2</sub>O<sub>4</sub>, have shown better electronic conductivity and higher reversible capacity than those of single-component metal oxides, which could be ascribed to the multiple aliovalent cations and corresponding more versatile redox reactions (Zhou et al., 2012; Li J. F. et al., 2013a,b,c; Chen et al., 2014c; Shen et al., 2014, 2015; Yuan et al., 2014; Zhang et al., 2014, 2015, 2016; Kang et al., 2015; Leng et al., 2015; Ma Y. et al., 2015; Ma Z. et al., 2015; Wang Y. K. et al., 2016; Wu L. J. et al., 2016; Yan et al., 2017). Among them, as a typical spinel structure, NiMn<sub>2</sub>O<sub>4</sub> has been extensively studied and demonstrated as a promising next generation anode material for LIBs (Kang et al., 2015; Ma Z. et al., 2015; Shen et al., 2015). However, the poor intrinsic electronic conductivity of NiMn<sub>2</sub>O<sub>4</sub> still impairs the electron transport kinetics during the process of the redox reaction, and NiMn<sub>2</sub>O<sub>4</sub> shows rapid capacity fading because of the slow ion-diffusion rates and large volume changes during the cycling process (Kang et al., 2015; Ma Y. et al., 2015; Ma Z. et al., 2015; Shen et al., 2015; Zhang et al., 2015).

To solve the aforementioned problems and enhance the electrochemical performance of transition metal oxides, one efficient method is to synthesize hollow multi-porous architecture of transition metal oxides (Zhou et al., 2012; Choi and Kang, 2013; Li J. F. et al., 2013a,b,c; Li Q. et al., 2013; Zhu et al., 2013a,b; Chen et al., 2014c; Luo S. et al., 2014; Pan et al., 2014; Wang L. Y. et al., 2014; Zhang et al., 2014, 2015, 2018; Gao et al., 2015; Kang et al., 2015; Leng et al., 2015; Ma Z. et al., 2015; Shen et al., 2015; Su et al., 2015; Wang Y. K. et al., 2016; Wu et al., 2018). Compared with bulk counterparts, the hollow multi-porous structures can provide enough void space to buffer architectural changes and alleviate the formation of the aggregate particles during the process of redox reactions (Li J. F. et al., 2013c; Li Q. et al., 2013; Zhang et al., 2014, 2015, 2018; Kang et al., 2015; Leng et al., 2015; Ma Z. et al., 2015; Shen et al., 2015; Wang Y. K. et al., 2016). In addition, the hollow multi-porous character is conducive to the electrolyte penetration, offering a short path for the lithium ions diffusion and electron-transportation (Li J. F. et al., 2013c; Li Q. et al., 2013; Gao et al., 2015; Zhang et al., 2015, 2018; Wang Y. K. et al., 2016).

Most recently, cation substitution has been certified to be an effective route to improve the electrical conductivity and charge transfer ability of the anode materials (Mai et al., 2011; Qiu et al., 2011; Li et al., 2012, 2015, 2016; Li Q. et al., 2013; Reddy et al., 2013; Suo et al., 2013; Chen et al., 2014a,b; Liu et al., 2014; Sun et al., 2014; Wang J. X. et al., 2014; Xu et al., 2014; Choi et al., 2015; He et al., 2015, 2017; Ma Z. et al., 2015; Mo et al., 2015; Jin et al., 2016; Wu F. X. et al., 2016; Wu L. J. et al., 2016). Ma Y. et al. (2015) found that the optimal level of iron doping in spinel NiMn<sub>2</sub>O<sub>4</sub> can improve the electrical conductivity and structural robustness and exhibit exciting lifespan. Tu et al. (Mai et al., 2011) found that “Co-doped NiO nanoflake arrays samples showed excellent rate capability and good capacity retention.” Furthermore, it is noted that the content of Co could also affect the structure and morphology of the transition metal oxides. Qian et al. (Li J. F. et al., 2013b) found that the distribution and morphology of MnCo<sub>2</sub>O<sub>4</sub> particles are very different from those of CoMn<sub>2</sub>O<sub>4</sub> particles. Typically, “the resultant pores are

much larger in CoMn<sub>2</sub>O<sub>4</sub> than that of MnCo<sub>2</sub>O<sub>4</sub>, possibly due to the longer transfer distance of ions” (Li J. F. et al., 2013b). These results imply that Co substitution is critical to the electrical conductivity and controlled porous architecture of transition metal oxides. However, to the best of our knowledge, the studies on Co substituted NiMn<sub>2</sub>O<sub>4</sub> mesocrystals with controlled phase structure and morphology are scarcely reported.

Herein, we first report a solvothermal method for the successful preparation of well-distributed hollow multi-porous superlattice NiMn<sub>2</sub>O<sub>4</sub>/NiCo<sub>2</sub>O<sub>4</sub> mesocrystals. As expected, Co element is uniformly distributed among the NiMn<sub>2</sub>O<sub>4</sub> mesocrystals, and that Co substitution induces a great evolution of the structure and morphology. The structure is changed from the single-phase NiMn<sub>2</sub>O<sub>4</sub> to a new mixed-phase NiMn<sub>2</sub>O<sub>4</sub>/NiCo<sub>2</sub>O<sub>4</sub> compound system. At the same time, the morphological transformation of the NiMn<sub>2</sub>O<sub>4</sub> sample to the Co-substituted samples take place in the significant conversion from irregular particles to well-distributed hollow multi-porous mesocrystals. The optimized NiCo<sub>1.5</sub>Mn<sub>0.5</sub>O<sub>4</sub> sample maintains 532.2 mAh g<sup>-1</sup> with 90.4% capacity retention after 100 cycles at a current density of 1 A g<sup>-1</sup> with the voltage of 0.01–3.00 V vs. Li/Li<sup>+</sup> at room temperature, because the superlattice NiMn<sub>2</sub>O<sub>4</sub>/NiCo<sub>2</sub>O<sub>4</sub> structure can enhance the charge transport kinetics, and the uniform hollow multi-porous architecture improve the structural stability and facilitate the electrolyte penetration during lithiation and delithiation cycling.

## EXPERIMENTAL

### Materials Synthesis

NiMn<sub>2-x</sub>Co<sub>x</sub>O<sub>4</sub> ( $x = 0, 0.5, 1, 1.5, 2$ ) oxide materials are synthesized by solvothermal reaction. The stoichiometric ratio of Ni(CH<sub>3</sub>COO)<sub>2</sub>·4H<sub>2</sub>O, Mn(CH<sub>3</sub>COO)<sub>2</sub>·2H<sub>2</sub>O, Co(CH<sub>3</sub>COO)<sub>2</sub>·2H<sub>2</sub>O, and hexamethylenetetramine (HMT) are dissolved in a mixed solvent of 13 mL water and 67 mL triethylene glycol (TEG) to obtain a homogeneous and transparent solution. Then the solution is put into a Teflon-lined stainless steel autoclave. After the autoclave is maintained at 200°C for 16 h, it is cooled to room temperature naturally. The precipitate is collected after filtration, washing, and drying to obtain the precursor. The as-prepared precursor is first calcinated at 250°C in air for 3 h and then at 900°C in air for 3 h.

NiMn<sub>2-x</sub>Co<sub>x</sub>O<sub>4</sub> ( $x = 0, 0.5, 1, 1.5, 2$ ) oxide materials, are labeled as NM ( $x = 0$ ), Co-1 ( $x = 0.5$ ), Co-2 ( $x = 1$ ), Co-3 ( $x = 1.5$ ), and Co-4 ( $x = 2$ ), respectively, and these corresponding precursors are labeled as NMP, CoP-1, CoP-2, CoP-3, and CoP-4, respectively.

### Materials Characterizations

X-ray diffraction (XRD, Rigaku D/Max 200PC, Japan) is employed to characterize the phases of all samples. The scanning range of diffraction angle ( $2\theta$ ) is 10°~90° and the scanning rate is 5° min<sup>-1</sup>. The morphologies of all samples are examined by scanning electron microscopy (SEM, Nova NanoSEM-230). The phase structures of the NM and Co-3 are analyzed by high resolution transmission electron microscopy (HRTEM, FEI Tecnai G2 F20 S-Twin working at 200 kV). The energy

dispersive X-ray spectroscopy (EDS) is used for the elemental characterization of all samples by OXFORD 7426 as the attachment of SEM, with the acceleration voltage of 20 kV. A specific surface area (SSA) analysis was used to measure material's BET SSA (SSAA, 3H2000, BSD, China).

## Electrochemical Measurement

The electrochemical tests are performed in CR2025 coin-type cells. Typical working electrode are prepared by a slurry coating process and the loadings are between 1.1 and 1.2 mg cm<sup>-2</sup>, and an electrode diameter of 10 mm is used. The working electrode consists of as-synthesized anode material, acetylene black and polyvinylidene difluoride (PVDF) binder with a weight ratio of 5:3:2. A lithium metal foil is used as the counter electrode. 1 M LiPF<sub>6</sub> dissolved in the mixtures of dimethyl carbonate (DMC), Ethyl Methyl Carbonate (EMC) and ethylene carbonate (EC) with a volume ratio of 1:1:1 is used as electrolyte. The assembly of the cells is carried out in a dry argon-filled MIKROUNA Universal 24401750 glovebox. Electrochemical performance of the materials are tested using an automatic galvanostatic charge-discharge unit, Land CT2001 battery cycler, in a cutoff voltage range within 0.01–3.0 V vs. Li/Li<sup>+</sup> at room temperature. The cyclic voltammetry (CV) are operated at a scan rate of 0.1 mV s<sup>-1</sup> in a cutoff voltage range within 0.01–3.0 V at room temperature with a CHI660D electrochemical analyzer. Finally, the electrochemical impedance spectroscopy (EIS) measurements are conducted by a CHI660D impedance analyzer, using 2-electrode cells. All cells are initially discharged and charged at a current density of 0.05 A g<sup>-1</sup>, and then discharged and charged different times of 1st and 100th at a current density of 1 A g<sup>-1</sup> with the voltage of 0.01 – 3.00 V vs. Li/Li<sup>+</sup> at room temperature. The amplitude voltage is 5 mV and the frequency range is 0.01–100,000 Hz.

## RESULTS AND DISCUSSION

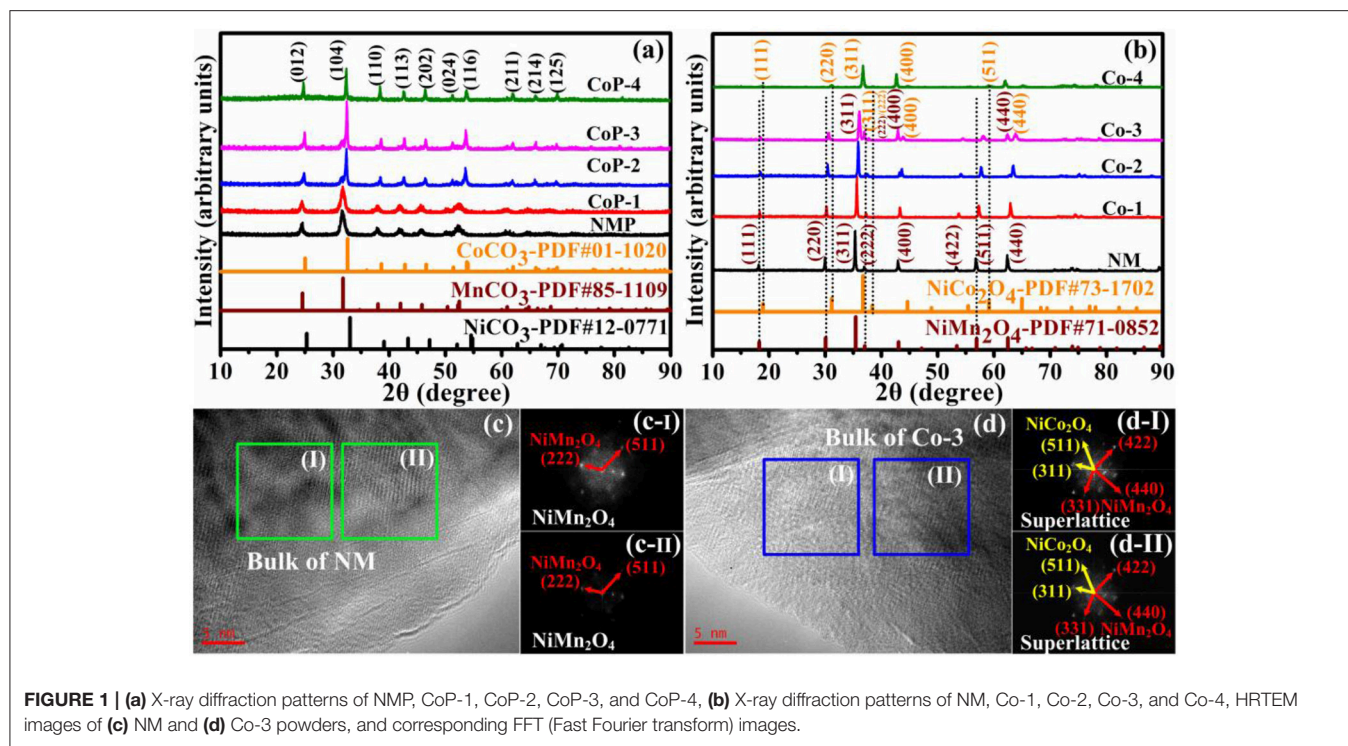
**Figure 1a** displays the X-ray diffraction patterns of the NMP, CoP-1, CoP-2, CoP-3, and CoP-4 precursors. Compared with standard XRD patterns of NiCO<sub>3</sub> (JCPDS no. 12-0771), MnCO<sub>3</sub> (JCPDS no. 85-1109), and CoCO<sub>3</sub> (JCPDS no. 01-1020), all the diffraction lines could be indexed on the basis of the hexagonal phase with the space group of R-3c (Qiu et al., 2011; Sun et al., 2014; Choi et al., 2015; Kang et al., 2015; Wu F. X. et al., 2016). With the increase of cobalt concentration, the manganese concentration decreases, and the diffraction peaks shift right to the positions at large angles, indicating that the substituted Co incorporates into the crystal lattice, resulting in the decrease of the lattice constant. Furthermore, from the diffraction lines of CoP-2 and CoP-3 precursors, it is noticed that a second phase appears in the pattern of the carbonate precursors at 2θ of about 32° and become obviously with the increase of the Co concentration, which can confirm that high cobalt concentrations prefer to form two phases rather than one phase (Ni<sub>1/3</sub>Mn<sub>2/3-x</sub>Co<sub>x</sub>CO<sub>3</sub>) in the carbonate precursors through the solvothermal process.

**Figure 1b** shows the X-ray diffraction patterns of the NM, Co-1, Co-2, Co-3, and Co-4 samples. The diffraction peaks of the NM

sample in the XRD patterns can be assigned to well-crystallized cubic spinel NiMn<sub>2</sub>O<sub>4</sub> (JCPDS no. 71-0852). Compared to that of the NM, the diffraction peaks of the Co-1 and Co-2 shift right to the positions at high diffraction angles, as the cobalt concentration increases, because the lattice constant is decreased by substituting Co<sup>3+</sup> (0.068 nm) into Mn<sup>3+</sup> (0.072 nm) site (Suo et al., 2013; Mo et al., 2015; He et al., 2017). Furthermore, from the diffraction line of Co-3, the distinct peaks of (311), (400), and (440) at 2θ of about 36, 43, and 64° are all completely separated, respectively, indicating a second cubic spinel phase of NiCo<sub>2</sub>O<sub>4</sub>, which is in accordance with the precursors results. These results suggest that the Co-3 is consistently made up of two phases, which allows hybridizing the phase of NiMn<sub>2</sub>O<sub>4</sub> with the phase of NiCo<sub>2</sub>O<sub>4</sub> into the architecture. In addition, the diffraction lines of Co-4 is assigned to CoO (JCPDS no. 70-2855) and NiCo<sub>2</sub>O<sub>4</sub> (JCPDS no. 73-1702), which might be ascribed that the single phase NiCo<sub>2</sub>O<sub>4</sub> cannot be synthesized through our heat-treat process. Chen et al. (Mo et al., 2015) reported that NiCo<sub>2</sub>O<sub>4</sub> is synthesized at 400°C with a temperature ramp of 4°C min<sup>-1</sup> and kept for 5 h under ambient air. However, in our study, Co-4 was first calcinated at 250°C in air for 3 h and then at 900°C in air for 3 h, which is consistency with the other samples.

To further confirm the effect of Co substitution on the microstructure of NiMn<sub>2</sub>O<sub>4</sub>, HRTEM and corresponding FFT (fast Fourier transform) images of NM and Co-3 samples are exhibited in **Figures 1c,d**. The lattice fringes and FFT patterns of both samples reveal that the NiMn<sub>2</sub>O<sub>4</sub> structure is successfully formed as expected. However, compared to that of NM (c-I and c-II), the corresponding FFTs of Co-3 (d-I and d-II) exhibit another two interplanar distances of 1.56 and 2.45 Å, which corresponds to the d-spacing of the (511) and (311) planes of NiCo<sub>2</sub>O<sub>4</sub> (JCPDS no. 73-1702), respectively. The NiMn<sub>2</sub>O<sub>4</sub> and NiCo<sub>2</sub>O<sub>4</sub> phases are mixing with one another at the atomic level in Co-3 particle, which suggests a two-phase composite nature of the sample derived from small fields of view. These results can determine that the Co-3 is a new mixed-phase NiMn<sub>2</sub>O<sub>4</sub>/NiCo<sub>2</sub>O<sub>4</sub> compound system with the presence of a superstructure. In addition, it is reported that the chemical composition of Ni and Co elements in NiCo<sub>2</sub>O<sub>4</sub> contains Ni<sup>2+</sup>/Ni<sup>3+</sup> and Co<sup>2+</sup>/Co<sup>3+</sup>, and the chemical composition of Ni and Mn elements in NiMn<sub>2</sub>O<sub>4</sub> contains Ni<sup>2+</sup>/Ni<sup>3+</sup> and Mn<sup>2+</sup>/Mn<sup>3+</sup> (Kang et al., 2015; Ma Y. et al., 2015; Mo et al., 2015; Shen et al., 2015; Li et al., 2016). Therefore, we hold this assumption that the chemical composition of Ni Co and Mn elements in NiCo<sub>1.5</sub>Mn<sub>0.5</sub>O<sub>4</sub> contains Ni<sup>2+</sup>/Ni<sup>3+</sup>, Co<sup>2+</sup>/Co<sup>3+</sup>, and Mn<sup>2+</sup>/Mn<sup>3+</sup>.

The SEM images of all carbonate precursors, corresponding EDS mappings of Ni, Co, Mn, and O for CoP-3 carbonate precursors and the EDX contents of Ni, Co and Mn element in all carbonate precursors are illustrated in **Figures 2a-j**. As can be seen in **Figures 2a,b**, the NMP and CoP-1 are composed by microflakes, microspheres and spindle-like particles. With the increase of Co concentration (**Figures 2c-e**), the microflakes disappear, and the microspheres are transformed into well-distributed spindle-like particles. EDS mapping result confirms that all elements, including Co, are uniformly distributed. EDX analysis exhibits that the ratio of Ni, Co and Mn element in



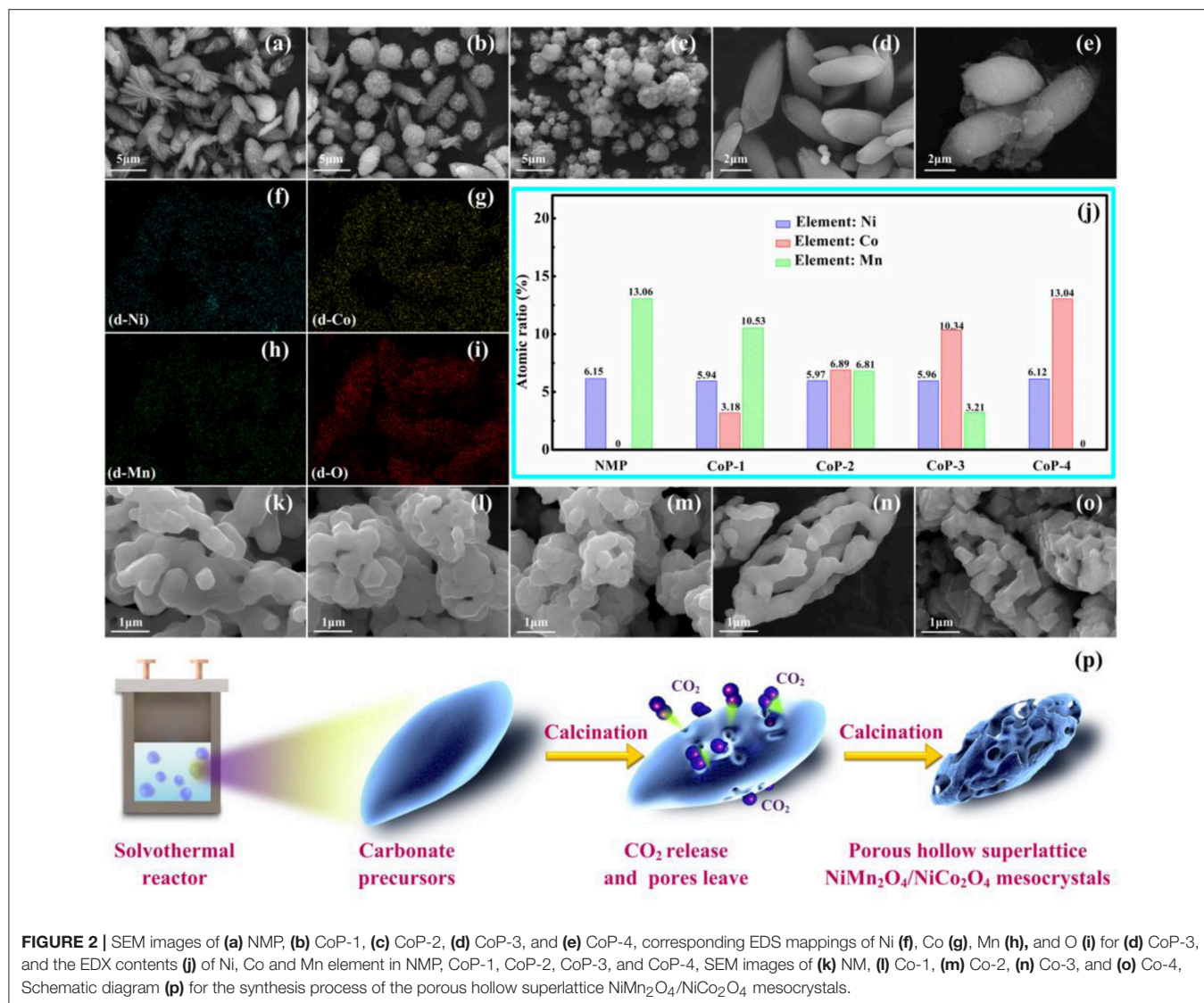
NMP, CoP-1, CoP-2, CoP-3, and CoP-4 is about 1:0:2, 1:0.5:1.5, 1:1:1, 1:1.5:0.5, 1:2:0, respectively, which is in accordance with our expectation. Therefore, it could be concluded that the stoichiometrical precursors are successfully synthesized via hydrothermal process, and that Co substitution is conducive to the good morphological consistency and distribution of the NMP particles.

The SEM images of all samples are illustrated in **Figures 2k–o** and Figure S1. Particles possessing porous character are observed for all the samples, which could be ascribed to the decomposition of carbonate precursor during heating process. It is also noted that the particles morphology for all the samples are inherited from those of the precursors. For example, particles from the NM sample show irregular morphology and random distribution. However, for the Co-1 and Co-2, the particles exhibit hollow spherical morphology and good distribution. As the increase of Co concentration, particles from the Co-3 exhibit spindle-like morphology and hollow multi-porous architecture. EDS mapping of Co-3 (Figure S1) shows a uniform distribution of Ni, Co, Mn, and O throughout the particle. These results confirm that Co incorporates into the Co-3, and Co substitution changes the morphology of both primary and aggregate particles, which might be benefit for lithium and electron diffusion during lithiation/delithiation reaction.

Schematic diagram for the synthesis process of the porous hollow superlattice NiMn<sub>2</sub>O<sub>4</sub>/NiCo<sub>2</sub>O<sub>4</sub> mesocrystals are illustrated in **Figure 2p**. The acetate molecules and hexamethylenetetramine dissolve in the solvent then gather together to form small droplets. During solvothermal treatment, the hexamethylenetetramine decomposes, and creates CO<sub>2</sub> bubbles. By capturing the metal ions on bubble surface, an

oval-like microsphere precursor is obtained successfully. During calcination process, metal ions move into crystal structure of the superlattice NiMn<sub>2</sub>O<sub>4</sub>/NiCo<sub>2</sub>O<sub>4</sub> mesocrystals, meanwhile, CO<sub>2</sub> release in the carbonate precursors, leaving pores on the obtained hollow complex oxides (Luo D. et al., 2014; Luo et al., 2015; Ma Z. et al., 2015; Shen et al., 2015).

To understand the oxidation/reduction and phase transformation processes in electrode reactions of the synthesized samples, the CV curves for the initial three cycles of NM and Co-3 samples are presented in **Figures 3A,B**, which are tested at a scan rate of 0.1 mV s<sup>-1</sup> in the voltage range of 0.01–3.00 V vs. Li/Li<sup>+</sup> at room temperature, respectively. The CV curves of both samples for the first cycle are significantly different from those for the following cycles, because of the irreversible electrochemical reaction during the first discharge cycle. However, no obvious alteration is observed between the second cycle and the third cycle, suggesting the good reversibility of lithium insertion and extraction reactions. In the first cycle, as can be seen in **Figure 3A**, there is a sharp reduction peak at 0.9 V and a broad reduction peak between 0.3 and 0.8 V. The sharp one associates with the initial reduction of Mn<sup>3+</sup>–Mn<sup>2+</sup>, and the broad one can be attributed to the reduction of NiMn<sub>2</sub>O<sub>4</sub> to metallic Mn and Ni and the formation of Li<sub>2</sub>O (Li J. F. et al., 2013b; Kang et al., 2015; Ma Y. et al., 2015; Ma Z. et al., 2015). With the increase of Co concentration (Figure S2), it is clear that the sharp reduction peak at 0.9 V is disappeared, and the reduction peaks which is attributed to the reduction of the oxides to metal and the formation of Li<sub>2</sub>O are narrower than that of NiMn<sub>2</sub>O<sub>4</sub>. In comparison, as shown in **Figure 3B**, a new reduction peak appear at 1.0 V, which can be corresponded to the reduction of Co<sup>3+</sup>–Co<sup>2+</sup>, and the broad reduction peaks



of Co-3 are completely separated. Yuan et al. (Ma Z. et al., 2015) and Lee et al. (Kang et al., 2015) reported that “the sharp peak at 0.5 V should correspond to the reduction of NiMn<sub>2</sub>O<sub>4</sub> to metallic Mn and Ni,” while Yang et al. (Zhang et al., 2016) and Wang et al. (Leng et al., 2015) reported that “the peak at 0.8 V should correspond to the reduction of NiCo<sub>2</sub>O<sub>4</sub> to metallic Co and Ni,” and both peaks “relate to the formation of Li<sub>2</sub>O and solid-electrolyte interface (SEI)” (Li J. F. et al., 2013c; Zhang et al., 2014, 2018; Gao et al., 2015). These results further confirm that Co-3 is a kind of mixed-phase NiMn<sub>2</sub>O<sub>4</sub>/NiCo<sub>2</sub>O<sub>4</sub> composite material, which is in accordance with the XRD results and TEM results as aforesaid. For the Co-3 sample, in the anodic sweep, a wide oxidation peak (~2.0 V) can be attributed to the oxidation of metals to oxides accompanying the decomposition of Li<sub>2</sub>O. Based on the above CV analysis, in conjunction with the previously reported storage mechanism for NiMn<sub>2</sub>O<sub>4</sub> and NiCo<sub>2</sub>O<sub>4</sub> (Li J. F. et al., 2013c; Zhang et al., 2014, 2016, 2018; Gao et al., 2015; Kang et al., 2015; Leng et al., 2015; Ma Y. et al., 2015;

Ma Z. et al., 2015; Su et al., 2015), the electrochemical reactions for the electrodes can be summarized as follows:

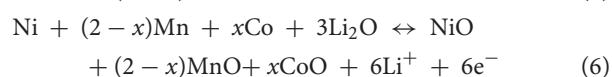
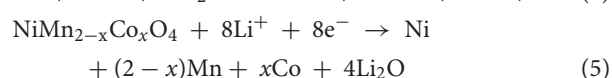
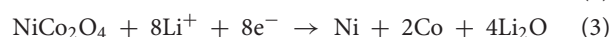
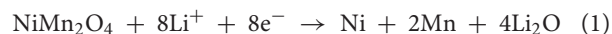


**Figure 3C** depicts the initial charge-discharge curves of the NM, Co-1, Co-2, Co-3, and Co-4 samples. The electrochemical tests are carried out at a current density of 0.05 A g<sup>-1</sup> with the voltage of 0.01–3.00 V vs. Li/Li<sup>+</sup> at room temperature. As can be seen in **Figure 3C**, there is a representative plateaus of the profile for

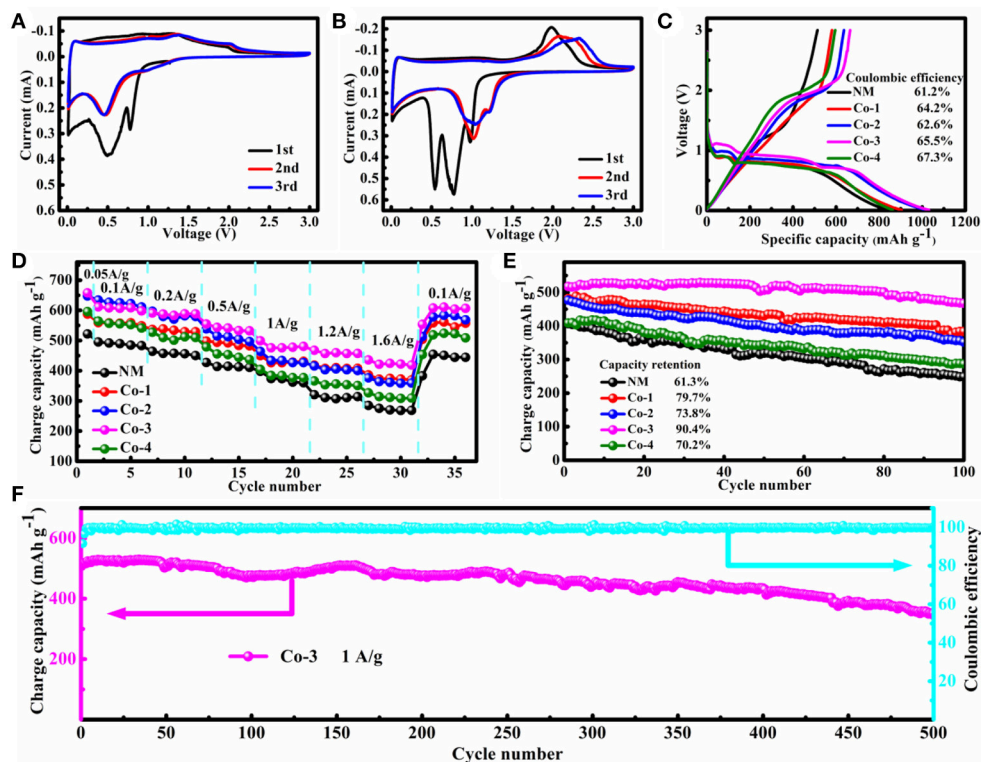


**FIGURE 3** | Electrochemical performance: (A) CV plots of NM, (B) CV plots of Co-3, (C) initial charge-discharge curves of NM, Co-1, Co-2, Co-3 and Co-4 (0.05 A g<sup>-1</sup>), (D) rate capability (0.05 A g<sup>-1</sup>–1.6 A g<sup>-1</sup>), (E) cyclic ability (1 A g<sup>-1</sup>) of all samples, (F) long-term cyclic ability of Co-3 (1 A g<sup>-1</sup>).

NM around 0.7 V in the first discharge process. By comparison, a representative profile of Co-3 which is composed of two plateaus around 0.9 V and 0.7 V in the first discharge process can be observed clearly, which relates to the insertion of lithium into the crystal structure of NiCo<sub>2</sub>O<sub>4</sub> and NiMn<sub>2</sub>O<sub>4</sub>, respectively, accompanied by the formation of Li<sub>2</sub>O (Wang J. X. et al., 2014; He et al., 2015, 2017; Mo et al., 2015; Li et al., 2016). The initial charge capacity for the NM, Co-1, Co-2, Co-3, and Co-4 is 513.5, 580.8, 636.9, 665.4, and 595.7 mAh g<sup>-1</sup>, respectively. It is obvious that the initial charge capacities of the Co-substituted samples are superior than that of the NM, particularly, the Co-3 sample exhibit the optimal initial charge capacities of all samples.

The rate capability of all samples are given in Figure 3D. The cells are charged/discharged at a current density of 0.05 A–1.6 A g<sup>-1</sup>, and then charged/discharged at a current density of 0.1 A g<sup>-1</sup> with the voltage of 0.01–3.00 V vs. Li/Li<sup>+</sup> at room temperature. It is noted that the Co-substituted samples show improved rate capability compared to the pristine counterparts at high rates. Specifically, the Co-3 demonstrates the best rate performance and delivers the highest reversible capacities of all samples. Remarkably, it can maintain the charge capacities of 611.4, 591.1, 554.6, 499.1, 467.6, 435.6, and 606.8 mAh g<sup>-1</sup> after 5 cycles at the current density of 0.1, 0.2, 0.5, 1, 1.2, 1.6, and 0.1 A g<sup>-1</sup>, respectively. Even at a current density as high as 1.6 A g<sup>-1</sup>, the Co-3 can still deliver a stable capacity of about 435.6 mAh g<sup>-1</sup> after 5 cycles, which is still higher than the theoretical

capacity of the graphite (372 mAh g<sup>-1</sup>), indicating the excellent rate capability.

The comparison of the cycling stability between the NM and the Co-substituted samples are presented in Figure 3E. The cells were charged/discharged 2 times at a current density of 0.05 A g<sup>-1</sup>, and then charged/discharged 100 times at a current density of 1 A g<sup>-1</sup> with the voltage of 0.01–3.00 V vs. Li/Li<sup>+</sup> at room temperature. The charge capacity retention reaches 61.3, 79.7, 73.8, 90.4, and 70.2% after 100 cycles for NM, Co-1, Co-2, Co-3, and Co-4, respectively. In particular, as can be seen in Figure 3F, the Co-3 maintains 532.2 mAh g<sup>-1</sup> with 67.8% capacity retention after 500 cycles at a current density of 1 A g<sup>-1</sup> with the voltage of 0.01–3.00 V vs. Li/Li<sup>+</sup> at room temperature. It means that the Co-3 can still deliver a stable capacity of about 360.8 mAh g<sup>-1</sup> after 500 cycles, which is still near the theoretical capacity of the graphite (372 mAh g<sup>-1</sup>), demonstrating the outstanding cycling stability. In conclusion, the porous Co-substituted samples in this work exhibit a superior electrochemical performance compared with the NM, specially, the Co-3 exhibits the optimal electrochemical performance of all samples.

To further understand the effects of the porous architecture on the electrochemical properties of Co-substituted samples, the Co-1 is selected as a reference, which has the similar structure but different morphological architecture, compared to the NM. The SEM images of NM and Co-1 electrodes

before and after 100 cycles are shown in **Figure 4**. The cells are charged to 3.00 V at high delithiation state. As can be seen in **Figure 4**, after 100 cycles, both samples (**Figures 4b,d**) show fuzzy surface, which may be due to the formation of Li<sub>2</sub>O and the electrolyte decomposition (Wang J. X. et al.,

2014; Mo et al., 2015; Li et al., 2016; He et al., 2017). Compared to the fresh electrode (**Figure 4a**), the irregular morphological NiMn<sub>2</sub>O<sub>4</sub> particles suffer serious damage and expand into aggregate particles after 100 cycles (**Figure 4b**). The aggregation can be ascribed to the volume expansion on

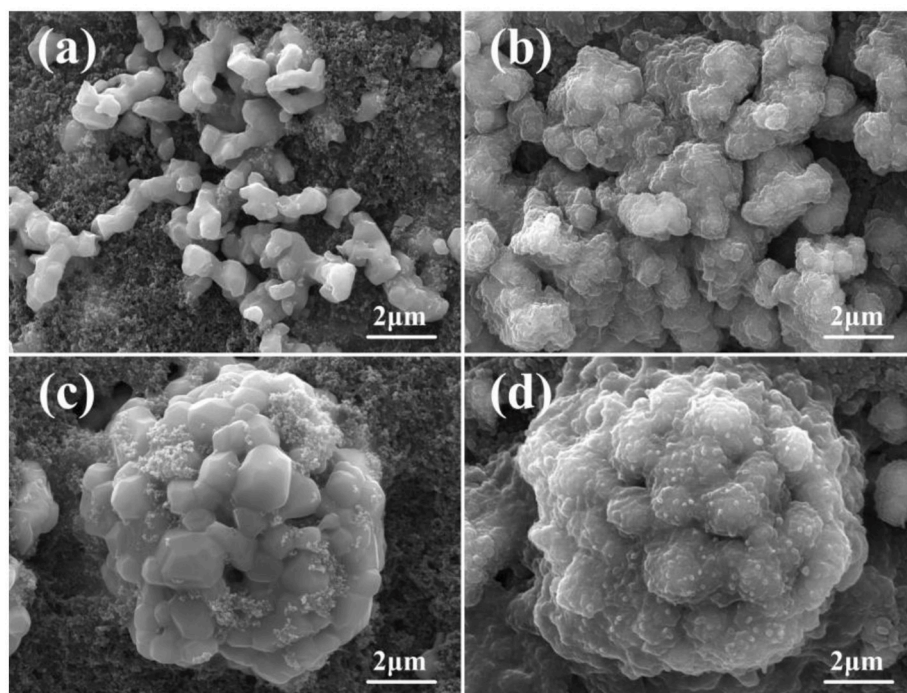


**FIGURE 4** | SEM images of (a,b) NM electrodes, (c,d) Co-1 electrodes, (a,c) before cycling, (b,d) after 100 cycles at a current density of 1A g<sup>-1</sup> with the voltage of 0.01–3.00 V vs. Li/Li<sup>+</sup>.

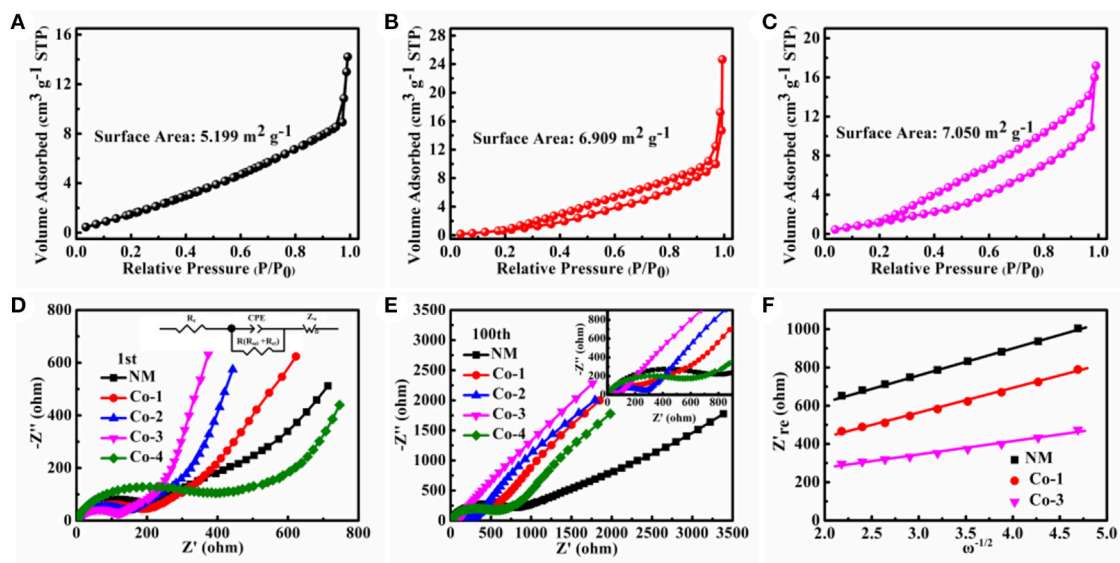


**FIGURE 5** | N<sub>2</sub> adsorption and desorption isotherm: (A) NM, (B) Co-1, and (C) Co-3. Nyquist plots of as-prepared electrodes, (D) after the 1st cycle and (E) after the 100th cycle, (F) the relationships between Z'<sub>re</sub> and ω<sup>-1/2</sup> after the 1st cycle for the NM, Co-1 and Co-3 electrodes.

account of the irreversible electrochemical process from the high lithiation state (Pan et al., 2014; Zhang et al., 2015). In contrast, for Co-1, as shown in **Figures 4c,d**, there is no obvious alteration in the hollow multi-porous particle morphology after 100 cycles. These results demonstrate that the hollow multi-porous architecture can provide enough void spaces to alleviate the architectural change, and offer a stable structure for the intercalation and de-intercalation cycling (Zhang et al., 2015). In addition, Nitrogen adsorption/desorption isotherms are shown in **Figures 5A–C**, the sorption isotherms are of type III isotherms, they have a distinct H3-type hysteresis loop in the range of  $P/P_0 = 0.2–0.99$ , which does not close until the saturation pressure is reached. Obviously, the BET specific surface area (SSA) of the Co-1 is  $6.909 \text{ m}^2 \text{ g}^{-1}$ , which is larger than that of the NM sample ( $5.199 \text{ m}^2 \text{ g}^{-1}$ ). The larger SSA can be derived from the hollow multi-porous architecture, leading to a shorter Li ions diffusion distance during the charge-discharge processes.

Furthermore, nyquist plots of the as-prepared electrodes and corresponding EIS and lithium ion diffusion coefficient ( $D_{\text{Li}^+}$ ) results are exhibited in **Tables 1, 2** and **Figures 5D–F**. The semicircle at high and intermediate frequency region relates the SEI film impedance ( $R_{\text{sei}}$ ) and the charge transfer impedance ( $R_{\text{ct}}$ ), respectively. The inclined straight line at the low frequency region is attributed to Warburg impedance ( $R_w$ ), which is associated with  $\text{Li}^+$  diffusion into the bulk (Qiu et al., 2011; Li et al., 2012; Chen et al., 2014a,b; Sun et al., 2014; Wang L. Y. et al., 2014; Xu et al., 2014; Choi et al., 2015; Wu F. X. et al., 2016; Wu et al., 2018). The lithium ion diffusion coefficient was calculated via a widely accepted method (Reddy et al., 2013; Li et al., 2015). With the increase of cycle number, it is obvious that the values of R for all samples rise. After 100 cycles, the resistance of all samples increase, and both samples (**Figures 4b,d**) show fuzzy surface. These results indicate that the SEI formed on the electrode. In addition, as shown in **Figures 4c,d**, there is no obvious alteration in the hollow multi-porous particle morphology after 100 cycles, which suggests that the uniform hollow multi-porous architecture can alleviate the pore size/function change originating from the volume expansion and the SEI formation during cycling. Specially, the

value of R for NM after 1 cycle and 100 cycles is 218.5 and  $719.3 \Omega$ , respectively, the dramatical increase of the resistance could be ascribed to the formation and expansion of aggregate particles (as seen in **Figure 4**), which is certainly harmful to electrolyte penetration and the lithium ions and electron transport. In comparison, the Co-substituted samples do not have significant changes, which should be attributed to that the hollow multi-porous architecture can provide enough void spaces to prevent particle aggregation, resulting in enhanced the charge transport kinetics during discharging/charging processes (Zhang et al., 2015). It is clear from the above discussions that the excellent rate capability and cycle stability of Co-substituted samples are attributed to the porous architecture by following factors: (1) provides enough void spaces to suppress the architectural collapse during cycle, (2) reduces the lithium ions diffusion and electron-transportation distances; (3) facilitates the electrolyte penetration resulting in enhanced the charge transport kinetics.

To further evaluate the effects of the superlattice structure on electrochemical properties of the NiMn<sub>2</sub>O<sub>4</sub>/NiCo<sub>2</sub>O<sub>4</sub>, the electrochemical kinetics of the Co-3 and Co-1 samples have been studied. The reason why choose Co-3 and Co-1 is partly due to the Co-3 exhibits superior electrochemical properties and superlattice structure, and partly due to Co-1 owns similar porous morphology with the Co-3, while is made up with a single phase. The BET results reveal that the SSA of the Co-1 and Co-3 samples is  $6.909$  and  $7.050 \text{ m}^2 \text{ g}^{-1}$ , respectively. The similar SSA means the similar Li ions diffusion distance during the charge-discharge process. Therefore, it is supposed that the electrochemical kinetic difference between the Co-1 and Co-3 mainly lies on structure. As shown in **Table 1**, the Co-3 exhibits the lowest initial R and the most stable resistance during cycling among all samples. Furthermore, it can be seen from **Table 2**, the  $D_{\text{Li}^+}$  of the Co-3 sample is  $1.19 \times 10^{-11} \text{ cm}^2 \text{ S}^{-1}$ , which is much higher than that of the Co-1 sample ( $3.49 \times 10^{-12} \text{ cm}^2 \text{ S}^{-1}$ ). Since the morphology and the SSA of the Co-1 is similar to those of Co-3, the superior electron and Li ion transport diffusive capacity of the Co-3 should be related to the superlattice NiMn<sub>2</sub>O<sub>4</sub>/NiCo<sub>2</sub>O<sub>4</sub> structure. A similar phenomenon has also been reported by Chen et al (Suo et al., 2013). They pointed out that the composite phases can supply high ionic conductivity. These results demonstrate that the superlattice NiMn<sub>2</sub>O<sub>4</sub>/NiCo<sub>2</sub>O<sub>4</sub> structure can facilitate the ionic conductivity to enhance charge transport kinetics of the bulk material.

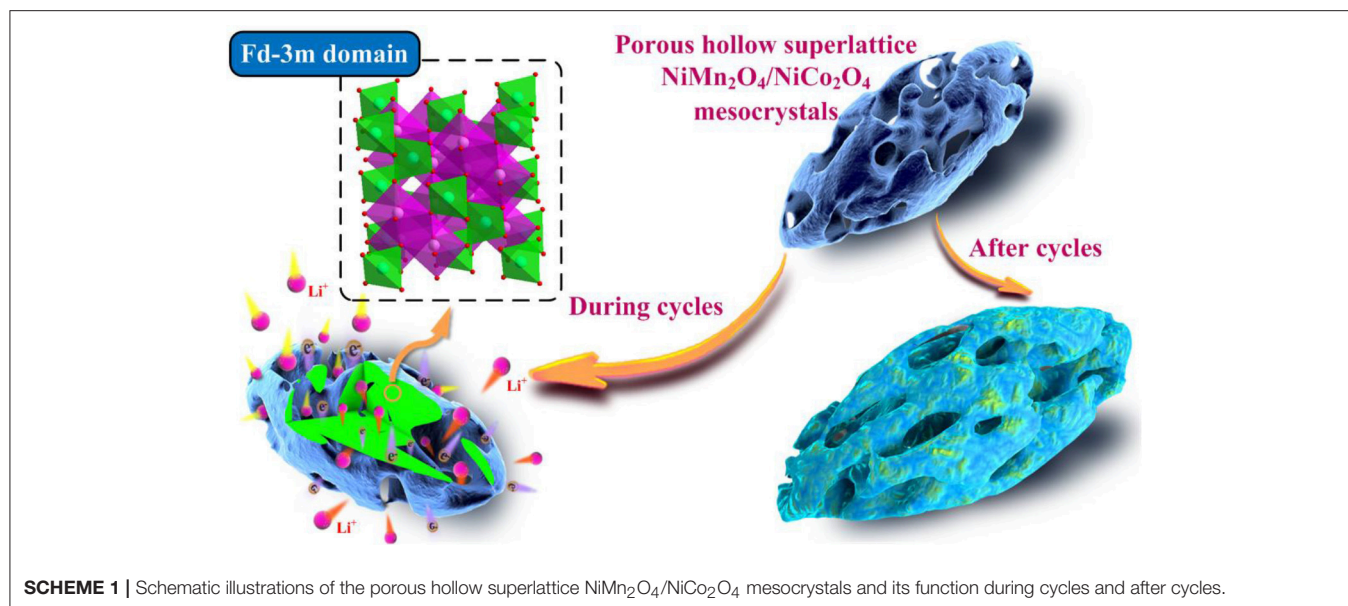
The schematic illustrations of the porous hollow superlattice NiMn<sub>2</sub>O<sub>4</sub>/NiCo<sub>2</sub>O<sub>4</sub> compound and the mechanism of electrochemical process are exhibited in **Scheme 1**. Many reports (Kang et al., 2015; Ma Y. et al., 2015; Ma Z. et al., 2015; Zhang et al., 2015, 2016) indicate that the aggregation from the irreversible volume expansion and the low charge transport kinetics, including the poor intrinsic electronic conductivity and the slow ion-diffusion rates, is responsible for the fading capacity of NiMn<sub>2</sub>O<sub>4</sub>. In this work, the porous hollow architecture can provide enough void spaces to suppress architectural collapse originating from the volume expansion during cycling, and offer a short stable path for the lithium

**TABLE 1** | The values of R for NM, Co-1, Co-2, Co-3 and Co-4 samples after the 1st and 100th cycle.

Samples	NM	Co-1	Co-2	Co-3	Co-4
1st ( $\Omega$ )	218.5	187.3	136.1	115.7	372.4
100th ( $\Omega$ )	791.3	277.1	281.5	127.6	568.2

**TABLE 2** | The values of specific surface area and  $D_{\text{Li}^+}$  for the NM and Co-3 samples.

Samples	NM	Co-1	Co-3
$D_{\text{Li}^+}(\text{cm}^2 \text{ S}^{-1})$	$2.99 \times 10^{-12}$	$3.49 \times 10^{-12}$	$1.19 \times 10^{-11}$
BET SSA ( $\text{m}^2 \text{ g}^{-1}$ )	5.199	6.909	7.050



ions diffusion and electron-transportation. Moreover, the superlattice NiMn<sub>2</sub>O<sub>4</sub>/NiCo<sub>2</sub>O<sub>4</sub> structure can facilitate the electronic and ionic conductivity to enhance charge transport kinetics of the bulk material. The synergistic effects of the superlattice NiMn<sub>2</sub>O<sub>4</sub>/NiCo<sub>2</sub>O<sub>4</sub> structure and the uniform hollow multi-porous architecture are guaranteed for the excellent electrochemical performance.

## CONCLUSIONS

In summary, the Co substituted NiMn<sub>2</sub>O<sub>4</sub> mesocrystals with controlled phase structure and morphology are successfully synthesized via a simple solvothermal method. The optimal sample with well-distributed hollow multi-porous superlattice NiMn<sub>2</sub>O<sub>4</sub>/NiCo<sub>2</sub>O<sub>4</sub> mesocrystals exhibits excellent rate ability and enhanced cycling performance, which maintains 532.2 mAh g<sup>-1</sup> with 90.4% capacity retention after 100 cycles, and can still deliver a stable capacity of about 360.8 mAh g<sup>-1</sup> after 500 cycles, at a current density of 1 A g<sup>-1</sup>. The excellent electrochemical performance can be attributed to the synergistic effect of the superlattice NiMn<sub>2</sub>O<sub>4</sub>/NiCo<sub>2</sub>O<sub>4</sub> structure and the uniform hollow multi-porous architecture. The superlattice structure can enhance the Li ion diffusion coefficient to enhance the charge transport kinetics. While, the uniform hollow multi-porous architecture can alleviate the architectural change originating from the volume expansion during cycling and facilitate electrolyte penetration. These combined effects

## REFERENCES

Chen, Y. J., Zhu, J., Qu, B. H., Lu, B., and Xu, Z. (2014a). Graphene improving lithium-ion battery performance by construction of NiCo<sub>2</sub>O<sub>4</sub>/graphene hybrid nanosheet arrays. *Nano Energy* 3, 88–94. doi: 10.1016/j.nanoen.2013.10.008

make the NiCo<sub>1.5</sub>Mn<sub>0.5</sub>O<sub>4</sub> a promising anode material for the practical application in EV/HEV and energy storage systems.

## AUTHOR CONTRIBUTIONS

LL and QY conceived the idea; QY and LL prepared all materials; QY, HY, and JL conducted SEM experiments; KY, BL, and ZL conducted XRD experiments; LL, QY, and BZ analyzed the data; QY wrote the manuscript and BZ, ZC, and JD commented on it; LL supervised the implementation of the project.

## ACKNOWLEDGMENTS

This work was financially supported by the National Natural Science Foundation of China (No. 51774051 and No. 51404156), the Changsha City Fund for Distinguished and Innovative Young Scholars (No. KQ1707014), Scientific Research Fund of Hunan Provincial Education Department (No. 17B002), the Key Laboratory of Efficient and Clean Energy Utilization, The Education Department of Hunan Province (No. 2016 NGQ005).

## SUPPLEMENTARY MATERIAL

The Supplementary Material for this article can be found online at: <https://www.frontiersin.org/articles/10.3389/fchem.2018.00153/full#supplementary-material>

Chen, Y. J., Zhuo, M., Deng, J. W., Xu, Z., Li, Q. H., and Wang T. H., (2014b). Reduced graphene oxide networks as an effective buffer matrix to improve the electrode performance of porous NiCo<sub>2</sub>O<sub>4</sub> nanoplates for lithium-ion batteries. *J. Mater. Chem. A* 2, 4449–4456. doi: 10.1039/c3ta14624c

- Chen, H. X., Zhang, Q. B., Wang, J. X., Wang, Q., Zhou, X., Li, X. H., et al. (2014c). Mesoporous ZnCo<sub>2</sub>O<sub>4</sub> microspheres composed of ultrathin nanosheets cross-linked with metallic NiSi<sub>x</sub> nanowires on Ni foam as anodes for lithium ion batteries. *Nano Energy* 10, 245–258. doi: 10.1016/j.nanoen.2014.09.020
- Choi, S. H., and Kang, Y. C. (2013). Yolk-shell, hollow, and single-crystalline ZnCo<sub>2</sub>O<sub>4</sub> powders: preparation using a simple one-pot process and application in lithium-ion batteries. *ChemSusChem* 6, 2111–2116. doi: 10.1002/cssc.201300300
- Choi, S. H., Park, S. K., Lee, J.-K., and Kang, Y. C. (2015). Facile synthesis of multi-shell structured binary metal oxide powders with a Ni/Co mole ratio of 1:2 for Li-Ion batteries. *J. Power Sources* 284, 481–488. doi: 10.1016/j.jpowsour.2015.03.026
- Gao, G. X., Wu, H. B., Ding, S. J., and Lou, X. W. (2015). Preparation of carbon-coated NiCo<sub>2</sub>O<sub>4</sub>@SnO<sub>2</sub> hetero-nanostructures and their reversible lithium storage properties. *Small* 11, 432–436. doi: 10.1002/smll.201400152
- Goodenough, J. B., and Park, K. S. (2013). The Li-Ion rechargeable battery: a perspective. *J. Am. Chem. Soc.* 135, 1167–1176. doi: 10.1021/ja3091438
- He, Z. J., Ping, J., Yi, Z. J., Peng, C., Shen, C. S., and Liu, J. S. (2017). Optimally designed interface of lithium rich layered oxides for lithium ion battery. *J. Alloy Compd.* 708, 1038–1045. doi: 10.1016/j.jallcom.2017.03.101
- He, Z. J., Wang, Z. X., Chen, H., Huang, Z. M., Li, X. H., Guo, H. J., et al. (2015). Electrochemical performance of Zr doped lithium rich layered Li<sub>1.2</sub>Mn<sub>0.54</sub>Ni<sub>0.13</sub>Co<sub>0.13</sub>O<sub>2</sub> oxide with porous hollow structure. *J. Power Sources* 299, 334–341. doi: 10.1016/j.jpowsour.2015.09.025
- Jin, R. C., Meng, Y. F., Ma, Y. Q., Li, H. H., Sun, Y. X., and Chen, G. (2016). Hierarchical MnCo<sub>2</sub>O<sub>4</sub> constructed by mesoporous nanosheets@polypyrrole composites as anodes for lithium ion batteries. *Electrochim. Acta* 209, 163–170. doi: 10.1016/j.electacta.2016.05.072
- Kang, K., Meng, Y. S., Breger, J., Grey, C. P., and Ceder, G. (2006). Electrodes with high power and high capacity for rechargeable lithium batteries. *Science* 311, 977–980. doi: 10.1126/science.1122152
- Kang, W. P., Tang, Y. B., Li, W. Y., Yang, X., Xue, H. T., Yang, Q. D., et al. (2015). High interfacial storage capability of porous NiMn<sub>2</sub>O<sub>4</sub>/C hierarchical tremella-like nanostructures as the lithium ion battery anode. *Nanoscale* 7, 225–231. doi: 10.1039/C4NR04031G
- Leng, X., Shao, Y., Wei, S. F., Jiang, Z. H., Lian, J. S., Wang, G. Y., et al. (2015). Ultrathin mesoporous NiCo<sub>2</sub>O<sub>4</sub> nanosheet networks as high-performance anodes for lithium storage. *ChemPlusChem* 80, 1725–1731. doi: 10.1002/cplu.201500322
- Li, J. F., Wang, J. Z., Liang, X., Zhang, Z. J., Liu, H. K., Qian, Y. T., et al. (2013a). Hollow MnCo<sub>2</sub>O<sub>4</sub> submicrospheres with multilevel interiors: from mesoporous spheres to yolk-in-double-shell structures. *ACS Appl. Mater. Interfaces* 6, 24–30. doi: 10.1021/am404841t
- Li, J. F., Xiong, S. L., Li, X. W., and Qian, Y. T. (2013b). A facile route to synthesize multiporous MnCo<sub>2</sub>O<sub>4</sub> and CoMn<sub>2</sub>O<sub>4</sub> spinel quasi-hollow spheres with improved lithium storage properties. *Nanoscale* 5, 2045–2054. doi: 10.1039/c2nr33576j
- Li, J. F., Xiong, S. L., Liu, Y. R., Ju, Z. C., and Qian, Y. T. (2013c). High electrochemical performance of monodisperse NiCo<sub>2</sub>O<sub>4</sub> mesoporous microspheres as anode material for Li-ion batteries. *ACS Appl. Mater. Interfaces* 5, 981–988. doi: 10.1021/am3026294
- Li, J. F., Xiong, S. L., Li, X. W., and Qian, Y. T. (2012). Spinel Mn<sub>1.5</sub>Co<sub>1.5</sub>O<sub>4</sub> core-shell microspheres as Li-ion battery anode materials with a long cycle life and high capacity. *J. Mater. Chem.* 22, 23254–23259. doi: 10.1039/c2jm35607d
- Li, L. J., Chen, Z. Y., Zhang, Q. B., Xu, M., Zhou, X., Zhu, H. L., et al. (2015). A hydrolysis-hydrothermal route for the synthesis of ultrathin LiAlO<sub>2</sub>-inlaid LiNi<sub>0.5</sub>Co<sub>0.2</sub>Mn<sub>0.3</sub>O<sub>2</sub> as a high-performance cathode material for lithium ion batteries. *J. Mater. Chem. A* 3, 894–904. doi: 10.1039/C4TA05902F
- Li, Q., Yin, L. W., Li, Z. Q., Wang, X. K., Qi, Y. X., and Ma, J. Y. (2013). Copper doped hollow structured manganese oxide mesocrystals with controlled phase structure and morphology as anode materials for lithium ion battery with improved electrochemical performance. *ACS Appl. Mater. Interfaces* 5, 10975–10984. doi: 10.1021/am403215j
- Li, T., Li, X. H., Wang, Z. X., Guo, H. J., Hu, Q. Y., and Peng, W. J. (2016). Robust synthesis of hierarchical mesoporous hybrid NiO–MnCo<sub>2</sub>O<sub>4</sub> microspheres and their application in Lithium-ion batteries. *Electrochim. Acta* 191, 392–400. doi: 10.1016/j.electacta.2016.01.113
- Liu, Y. J., Gao, Y. Y., Wang, Q. L., and Dou, A. C. (2014). Improvement of electrochemical performance of layered manganese enriched electrode material with the coating of Ni<sub>0.25</sub>Mn<sub>0.75</sub>O<sub>x</sub> composite oxides. *J. Alloy Compd.* 605, 1–6. doi: 10.1016/j.jallcom.2014.03.172
- Liu, Y. J., Wang, Q. L., Gao, Y. Y., Pan, J., Su, M. R., and Hai, B. (2015). Effect of cooling method on the electrochemical performance of layered-spinel composite cathode Li<sub>1.1</sub>Ni<sub>0.25</sub>Mn<sub>0.75</sub>O<sub>2.3</sub>. *J. Alloy Compd.* 646, 112–118. doi: 10.1016/j.jallcom.2015.06.024
- Luo, D., Fang, S. H., Tian, Q. H., Qu, L., Shen, S. M., Yang, L., et al. (2015). Uniform LiMO<sub>2</sub> assembled microspheres as superior cycle stability cathode materials of high energy and power Li-ion batteries. *J. Mater. Chem. A* 3, 22026–22030. doi: 10.1039/C5TA06592E
- Luo, D., Li, G. S., Fu, C. C., Zheng, J., Fan, J. M., Li, Q., et al. (2014). A new spinel-layered li-rich microsphere as a high-rate cathode material for li-ion batteries. *Adv. Energy Mater.* 4:1400062. doi: 10.1002/aenm.201400062
- Luo, S., Wu, H. C., Wu, Y., Jiang, K. L., Wang, J. P., and Fan, S. S. (2014). Mn<sub>3</sub>O<sub>4</sub> nanoparticles anchored on continuous carbon nanotube network as superior anodes for lithium ion batteries. *Power Sources J.* 249, 463–469. doi: 10.1016/j.jpowsour.2013.10.133
- Ma, Y., Tai, C. W., Younesi, R., Gustafsson, T., Lee, J. Y., and Edström, K. (2015). Iron doping in spinel NiMn<sub>2</sub>O<sub>4</sub>: stabilization of the mesoporous cubic phase and kinetics activation toward highly reversible Li<sup>+</sup> storage. *Chem. Mater.* 27, 7698–7709. doi: 10.1021/acs.chemmater.5b03288
- Ma, Z., Yuan, X. X., Li, L., Ma, Z. F., Zhang, L., Mai, L. Q., et al. (2015). Porous Ni<sub>0.14</sub>Mn<sub>0.86</sub>O<sub>1.43</sub> hollow microspheres as high-performing anodes for lithium-ion batteries. *J. Power Sources* 291, 156–162. doi: 10.1016/j.jpowsour.2015.05.021
- Mai, Y. J., Tu, J. P., Xia, X. H., Gu, C. D., and Wang, X. L. (2011). Co-doped NiO nanoflake arrays toward superior anode materials for lithium ion batteries. *J. Power Sources* 196, 6388–6393. doi: 10.1016/j.jpowsour.2011.03.089
- Mo, Y. D., Ru, Q., Song, X., Hu, S. J., Guo, L. Y., and Chen, X. Q. (2015). 3-dimensional porous NiCo<sub>2</sub>O<sub>4</sub> nanocomposite as a high-rate capacity anode for lithium-ion batteries. *Electrochim. Acta* 176, 575–585. doi: 10.1016/j.electacta.2015.07.049
- Pan, A. Q., Wang, Y. P., Xu, W., Nie, Z. W., Liang, S. Q., Zhang, J. G., et al. (2014). High-performance anode based on porous Co<sub>3</sub>O<sub>4</sub> nanodiscs. *J. Power Sources* 255, 125–129. doi: 10.1016/j.jpowsour.2013.12.131
- Qiu, Y. C., Xu, G. L., Yan, K. Y., Sun, H., Xiao, J. W., Yang, S. H., et al. (2011). Morphology-conserved transformation: synthesis of hierarchical mesoporous nanostructures of Mn<sub>2</sub>O<sub>3</sub> and the nanostructural effects on Li-ion insertion/de-insertion properties. *J. Mater. Chem.* 21, 6346–6353. doi: 10.1039/c1jm00011j
- Reddy, M. V., Rao, G. V. S., and Chowdari, B. V. R. (2013). Metal oxides and oxyals as anode materials for li ion batteries. *Chem. Rev.* 113, 5364–5457. doi: 10.1021/cr3001884
- Scrosati, B., Hassoun, J., and Sun, Y.-K. (2011). Lithium-ion batteries. A look into the future. *Energy Environ. Sci.* 4, 3287–3295. doi: 10.1039/c1ee01388b
- Shen, L. F., Che, Q., Li, H. S., and Zhang, X. G. (2014). Mesoporous NiCo<sub>2</sub>O<sub>4</sub> nanowire arrays grown on carbon textiles as binder-free flexible electrodes for energy storage. *Adv. Funct. Mater.* 24, 2630–2637. doi: 10.1002/adfm.201303138
- Shen, L. F., Yu, L., Yu, X. Y., Zhang, X. G., and Lou, X. W. (2015). Self-templated formation of uniform NiCo<sub>2</sub>O<sub>4</sub> hollow spheres with complex interior structure for lithium-ion batteries and supercapacitors. *Angew. Chem. Int. Ed.* 54, 1868–1872. doi: 10.1002/anie.201409776
- Su, L. W., Wu, X. B., Hei, J. P., Wang, L. B., and Wang, Y. H. (2015). Mesoporous Mn<sub>3</sub>O<sub>4</sub> nanobeads/graphene hybrids: facile gel-like film synthesis, rational structure design, and excellent performance for lithium storage. *Part. Part. Syst. Charact.* 32, 721–727. doi: 10.1002/ppsc.201500002
- Su, M. R., Wan, H. F., Liu, Y. J., Xiao, W., Dou, A. C., Wang, Z. X., et al. (2018). Multi-layered carbon coated Si-based composite as anode for lithium-ion batteries. *Powder Technol.* 323, 294–300. doi: 10.1016/j.powtec.2017.09.005
- Sun, H. T., Sun, X., Hu, T., Yu, M. P., Lu, F. Y., and Lian, J. (2014). Graphene-wrapped mesoporous cobalt oxide hollow spheres anode for high-rate and long-life lithium ion batteries. *J. Phys. Chem. C* 118, 2263–2272. doi: 10.1021/jp408021m
- Suo, L. M., Hu, Y. S., Li, H., Armand, M., and Chen, L. Q. (2013). A new class of solvent-in-salt electrolyte for high-energy rechargeable metallic lithium batteries. *Nat. Commun.* 4:1481. doi: 10.1038/ncomms2513

- Wang, J. X., Liu, Z. M., Yan, G. C., Li, H. K., Peng, W. J., Li, X. H., et al. (2016). Improving the electrochemical performance of lithium vanadium fluorophosphate cathode material: focus on interfacial stability. *J. Power Sources* 329, 553–557. doi: 10.1016/j.jpowsour.2016.08.131
- Wang, J. X., Zhang, Q. B., Li, X. H., Xu, D. G., Wang, Z. X., Guo, H. J., et al. (2014). Three-dimensional hierarchical Co<sub>3</sub>O<sub>4</sub>/CuO nanowire heterostructure arrays on nickel foam for high-performance lithium ion batteries. *Nano Energy* 6, 19–26. doi: 10.1016/j.nanoen.2014.02.012
- Wang, L. Y., Zhuo, L. H., Zhang, C., and Zhao, F. Y. (2014). Embedding NiCo<sub>2</sub>O<sub>4</sub> nanoparticles into a 3DHPC assisted by CO<sub>2</sub>-expanded ethanol: a potential lithium-ion battery anode with high performance. *ACS Appl. Mater. Interfaces* 6, 10813–10820. doi: 10.1021/am502812b
- Wang, Y. K., Wang, S. J., Zhao, T. T., Chen, Y., Li, Z. T., Wu, W. T., et al. (2016). Firmly combination of CoMnO<sub>x</sub> nanocrystals supported on N-doped CNT for lithium-ion batteries. *Chem. Eng. J.* 306, 336–343. doi: 10.1016/j.cej.2016.07.071
- Wu, F. X., Lee, J. T., Zhao, E. B., Zhang, B., and Yushin, G. (2016). Graphene-Li<sub>2</sub>S-carbon nanocomposite for lithium-sulfur batteries. *ACS Nano* 10, 1333–1340. doi: 10.1021/acsnano.5b06716
- Wu, L., Hu, Y., Zhang, X. P., Liu, J. Q., Zhu, X., and Zhong, S. K. (2018). Synthesis of carbon-coated Na<sub>2</sub>MnPO<sub>4</sub>F hollow spheres as a potential cathode material for Na-ion batteries. *J. Power Sources* 374, 40–47. doi: 10.1016/j.jpowsour.2017.11.029
- Wu, L. J., Lang, J. W., Wang, S., Zhang, P., and Yan, X. B. (2016). Study of Ni-doped MnCo<sub>2</sub>O<sub>4</sub> Yolk-Shell Submicron-spheres with Fast Li<sup>+</sup> Intercalation Pseudocapacitance As An Anode for High-Performance Lithium Ion Batteries. *Electrochim. Acta* 203 128–135. doi: 10.1016/j.electacta.2016.04.036
- Wu, X. W., Xiang, Y. H., Peng, Q. J., Wu, X. S., Li, Y. H., Tang, F., et al. (2017). Green-low-cost rechargeable aqueous zinc-ion batteries using hollow porous spinel ZnMn<sub>2</sub>O<sub>4</sub> as the cathode material. *J. Mater. Chem. A* 5, 17990–17997. doi: 10.1039/C7TA00100B
- Xie, K. Y., Lu, Z. G., Huang, H. T., Lu, W., Lai, Y. Q., Li, J., et al. (2012). Iron supported C@Fe<sub>3</sub>O<sub>4</sub> nanotube array: a new type of 3D anode with low-cost for high performance lithium-ion batteries. *J. Mater. Chem.* 22, 5560–5567. doi: 10.1039/c2jm15955d
- Xu, X., Dong, B. T., Ding, S. J., Xiao, C. H., and Yu, D. M. (2014). Hierarchical NiCoO<sub>2</sub> nanosheets supported on amorphous carbon nanotubes for high-capacity lithium-ion batteries with a long cycle life. *J. Mater. Chem. A* 2, 13069–13074. doi: 10.1039/C4TA02003K
- Yan, Z. L., Hu, Q. Y., Yan, G. C., Li, H. K., Shih, K., Yang, Z. W., et al. (2017). Co<sub>3</sub>O<sub>4</sub>/Co nanoparticles enclosed graphitic carbon as anode material for high performance Li-ion batteries. *Chem. Eng. J.* 321, 495–501. doi: 10.1016/j.cej.2017.03.146
- Yuan, C. Z., Wu, H. B., Xie, Y., and Lou, X. W. (2014). Mixed transition-metal oxides: design, synthesis, and energy-related applications. *Angew. Chem. Int. Ed.* 53, 1488–1504. doi: 10.1002/anie.201303971
- Zhang, Q. B., Chen, H. X., Han, X., Cai, J. J., Yang, Y., Liu, M. L., et al. (2016). Graphene-encapsulated nanosheet-assembled Zinc-Nickel-Cobalt Oxide microspheres for enhanced lithium storage. *ChemSusChem* 9, 186–196. doi: 10.1002/cssc.201501151
- Zhang, Q. B., Chen, H. X., Luo, L. L., Zhao, B. T., Luo, H., Han, X., et al. (2018). Harnessing the concurrent reaction dynamics in active Si and Ge to achieve high performance lithium-ion batteries. *Energy Environ. Sci.* 11, 669–681. doi: 10.1039/C8EE00239H
- Zhang, Q. B., Chen, H. X., Wang, J. X., Xu, D. G., Li, X. H., Yang, Y., et al. (2014). Growth of hierarchical 3D mesoporous NiSi<sub>x</sub>/NiCo<sub>2</sub>O<sub>4</sub> Core/Shell heterostructures on nickel foam for lithium-ion batteries. *ChemSusChem* 7, 2325–2334. doi: 10.1002/cssc.201402039
- Zhang, Q. B., Wang, J. X., Dong, J. C., Ding, F., Li, X. H., Zhang, B., et al. (2015). Facile general strategy toward hierarchical mesoporous transition metal oxides arrays on three-dimensional macroporous foam with superior lithium storage properties. *Nano Energy* 13, 77–91. doi: 10.1016/j.nanoen.2015.01.029
- Zhou, L., Zhao, D., and Lou, X. W. (2012). Double-Shelled CoMn<sub>2</sub>O<sub>4</sub> hollow microcubes as high-capacity anodes for lithium-ion batteries. *Adv. Mater.* 24, 745–748. doi: 10.1002/adma.201104407
- Zhu, X. D., Tian, J., Le, S. R., Chen, J. R., and Sun, K. N. (2013a). Enhanced electrochemical performances of CuCrO<sub>2</sub>-CNTs nanocomposites anodes by *in-situ* hydrothermal synthesis for lithium ion batteries. *Mater. Lett.* 107, 147–149. doi: 10.1016/j.matlet.2013.05.137
- Zhu, X. D., Tian, J., Le, S. R., Zhang, N. Q., and Sun, K. N. (2013b). Improved electrochemical performance of CuCrO<sub>2</sub> anode with CNTs as conductive agent for lithium ion batteries. *Mater. Lett.* 97, 113–116. doi: 10.1016/j.matlet.2013.01.103

**Conflict of Interest Statement:** The authors declare that the research was conducted in the absence of any commercial or financial relationships that could be construed as a potential conflict of interest.

The reviewer, BQ, and handling Editor declared their shared affiliation.

Copyright © 2018 Li, Yao, Liu, Ye, Liu, Liu, Yang, Chen, Duan and Zhang. This is an open-access article distributed under the terms of the Creative Commons Attribution License (CC BY). The use, distribution or reproduction in other forums is permitted, provided the original author(s) and the copyright owner are credited and that the original publication in this journal is cited, in accordance with accepted academic practice. No use, distribution or reproduction is permitted which does not comply with these terms.